Femtosecond pulse amplification on a chip

Mahmoud A. Gaafar[1,*], Markus Ludwig[1,*], Kai Wang[2], Thibault Wildi[1], Thibault Voumard [1], Milan Sinobad[1], Jan Lorenzen[1], Henry Francis[3], Jose Carreira[3], Shuangyou Zhang[4], Toby Bi[4,5], Pascal Del'Haye[4,5], Michael Geiselmann[3], Neetesh Singh[1], Franz X. Kärtner[1,6], Sonia M. Garcia-Blanco[2], Tobias Herr[1,6,**]

[1]Deutsches Elektronen-Synchrotron DESY, Notkestr. 85, 22607 Hamburg, Germany
[2]Integrated Optical Systems, MESA+ Institute for Nanotechnology, University of Twente, 7500AE, Enschede, The Netherlands
[3]LIGENTEC SA, EPFL Innovation Park, Chemin de la Dent-d'Oche 1B, Switzerland CH-1024 Ecublens, Switzerland
[4] Max-Planck Institute for the Science of Light, 91058 Erlangen, Staudtstr. 2, Germany
[5] Department of Physics, FAU Erlangen-Nürnberg, 91058 Erlangen, Germany
[6] Department of Physics, Universität Hamburg, Luruper Chaussee 149, 22761 Hamburg, Germany
[*]These authors contributed equally.
[**]tobias.herr@desy.de

Femtosecond laser pulses enable the synthesis of light across the electromagnetic spectrum and provide access to ultrafast phenomena in physics, biology, and chemistry. Chip-integration of femtosecond technology could revolutionize applications such as point-of-care diagnostics, biomedical imaging, portable chemical sensing, or autonomous navigation. However, current chip-integrated pulse sources lack the required peak power and on-chip amplification of femtosecond pulses has been an unresolved challenge. Here, addressing this challenge, we report >50-fold amplification of 1 GHz-repetition-rate chirped femtosecond pulses in a CMOS-compatible photonic chip to 800 W peak power with 116 fs pulse duration. This power level is 2-3 orders of magnitude higher compared to those in previously demonstrated on-chip pulse sources and can provide the power needed to address key applications. To achieve this, detrimental nonlinear effects are mitigated through all-normal dispersion, large mode-area and rare-earth-doped gain waveguides. These results offer a pathway to chip-integrated femtosecond technology with peak power-levels characteristic of table-top sources.

Introduction

Femtosecond laser pulses with high-peak power are a fundamental resource in photonics. By temporally concentrating laser light, they provide unique access to ultrashort time-scales and nonlinear optical effects and have found applications across many disciplines including biomedical imaging [1–3], femtochemistry [4, 5], optical precision spectroscopy, molecular sensing, low-noise signal generation and time keeping [6–8]. Recent developments of photonic-chip integration of femtosecond sources via microresonators [9–11], on-chip mode-locked lasers [12–15], and integrated electro-optic pulse generators [16], have created tremendous opportunities for femtosecond technology to become accessible at low-cost with high-volume, compact footprint and beyond specialized laboratories. These developments hold potential for large-scale societal benefits such as advanced point-of-care diagnostics, distributed environmental monitoring, and mobile application such as signal generation for navigation and communication. A current roadblock, however, is the low output peak power of chip-integrated femtosecond sources (around 1 W, or much below that), which is often too low for their envisioned application. Thus, almost all proof-of-concept demonstrations with ultrashort pulses from on-chip sources have critically relied on table-top optical amplifiers. Integrating these pulse amplifiers on a chip, is a long standing challenge.

Previous work has already demonstrated chip-integrated (quasi-) continuous-wave amplifiers based on rare-earth-doped waveguides [17–26] sustaining power levels up to 1 W [27], heterogeneous semiconductor integration [28–31] or nonlinear parametric gain [32–34]. However, the amplification of femtosecond pulses in an integrated photonics setting has remained challenging, with nonlinear pulse distortion already at low peak power levels of 20 W [25]. Indeed, the strong light confinement in integrated waveguides results in strong nonlinearities, typically 1000-times higher than those in optical fibers. While often advantageous [35], e.g. for broadband supercontinua [36–39], nonlinear optical effects during the amplification process can lead to the irreversible degradation of the pulse within sub-mm propagation distances.

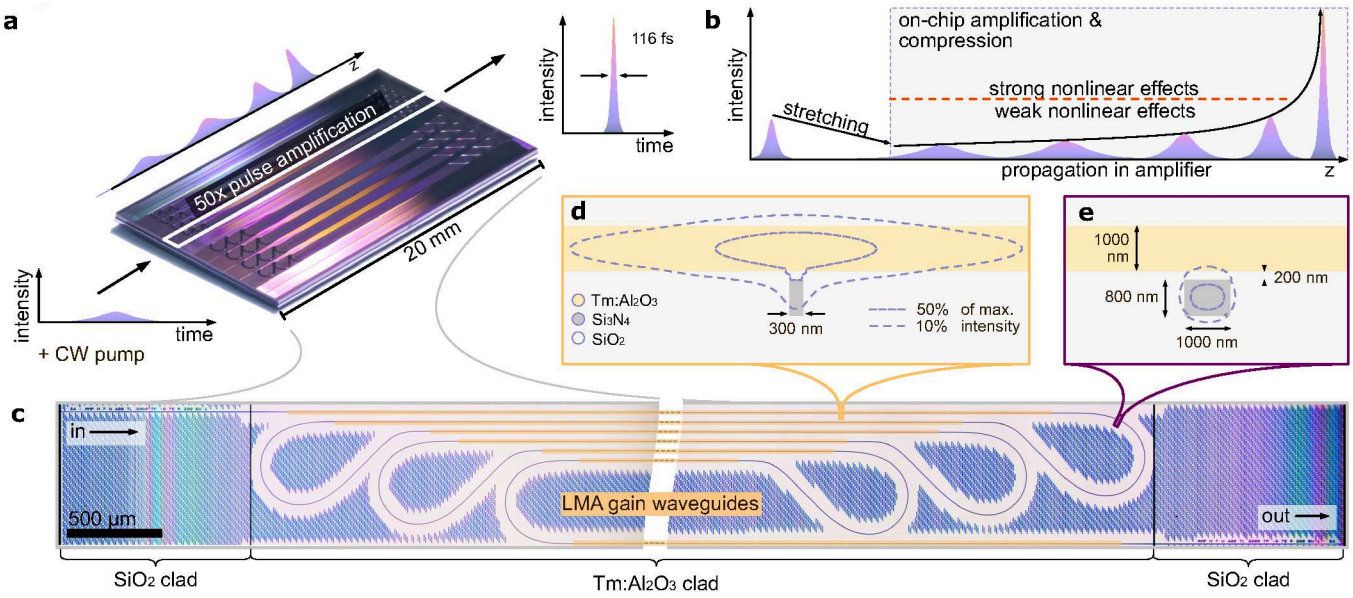

Figure 1 | Ultrafast pulse amplification on a chip. **a**, Photograph of the chip, hosting several amplifiers. Low energy chirped pulses are amplified 50-fold. The output pulse is a high-peak power, nearly time-bandwidth-limited femtosecond pulse. **b**, After temporally stretching (chirping) the input pulse, it is coupled to the amplifier chip, where it is gradually amplified and compressed, avoiding strong nonlinearities until passing the output section. **c**, Composite photograph of an amplifier structure, consisting of large mode-area (LMA) gain waveguides, folded into a small 15 mm^2-scale footprint. The waveguides are defined in a silicon nitride (Si_3N_4) layer, where within the area of the gain waveguides, an active thulium-doped alumina layer (Tm^{3+}:Al_2O_3) is used as a top cladding; in the input and output sections a silica (SiO_2) cladding is used. **d**, Layer structure in the LMA gain waveguide section. Intensity contours of the optical mode illustrate that most of the power is propagating in the gain layer for optimal amplification. **e**, Same as (d) but for the bent waveguide sections. The mode is strongly confined to the Si_3N_4-core, enabling low loss propagation through the bends.

Tabletop laser systems have historically faced a similar challenge. Nonlinear optical effects would prevent the amplification of pulses or even result in damage of the amplifier itself [40]. A major breakthrough came through the demonstration of *chirped pulse amplification* (CPA) [41]. In CPA the pulse is temporally stretched (*chirped*) to lower its peak power, amplified, and then temporally re-compressed only after amplification. While stretching can be readily accomplished at low power levels through a dispersive optical element, amplification and compression require advanced optical setups to manage nonlinearity, group velocity dispersion (GVD), and for ultra-short pulses, also higher-order dispersion.

Here, we demonstrate femtosecond pulse amplification on an integrated photonic chip to hundreds of Watts of peak power (Fig. 1a), a previously lacking cornerstone for chip-scale femtosecond technology. Our approach pursues a concept that resembles CPA to mitigate the strong nonlinear optical effects that are usually associated with integrated photonics. Pre-chirped input pulses propagating through the amplifier are simultaneously amplified and temporally compressed by managing nonlinearity and dispersion so that ultrashort pulse duration and high-pulse peak power are reached at the amplifier's output facet (Fig. 1b). In this way, we achieve >50-fold amplification of ultrashort pulses from a 1 GHz femtosecond source (center wavelength 1815 nm) to 800 W peak power and a final pulse duration of 116 fs. Our experimental results are in excellent agreement with a numerical pulse propagation model that includes the dynamics of the Tm-doped gain medium.

Results

The amplifier (Fig. 1c) is fabricated in a CMOS-compatible, scalable silicon nitride (Si_3N_4) photonic-chip platform (here with a 800 nm thick waveguide layer). The total length of the amplifier waveguide structure is 12 cm, which is integrated in a 15 mm^2-scale footprint. It comprises a total of ~10 cm of straight waveguide sections that provide gain and curved waveguide sections for compact integration. To achieve on-chip gain, the silica (SiO_2) top cladding is selectively removed in the amplifier section down to 200 nm above the Si_3N_4 layer. In a next step, a 1000 nm thick thulium-doped alumina (Tm^{3+}:Al_2O_3) gain layer is deposited. The refractive index of the gain layer $n \approx 1.72$ is between that of Si_3N_4 and SiO_2. The estimated Tm concentration is $3.5{\cdot}10^{20}cm^{-3}$. A 1000 nm-thick silica layer is deposited on top for protection (see Methods for more details on fabrication). In the straight gain sections the width of the Si_3N_4 waveguide is reduced to 300 nm, resulting in a single-mode waveguide with large mode-area that is mostly contained in the active alumina gain layer (Fig. 1d). Such large mode area (LMA) gain waveguides [14] can provide high-gain per unit length, low-nonlinearity, and high saturation power [27], and have al-

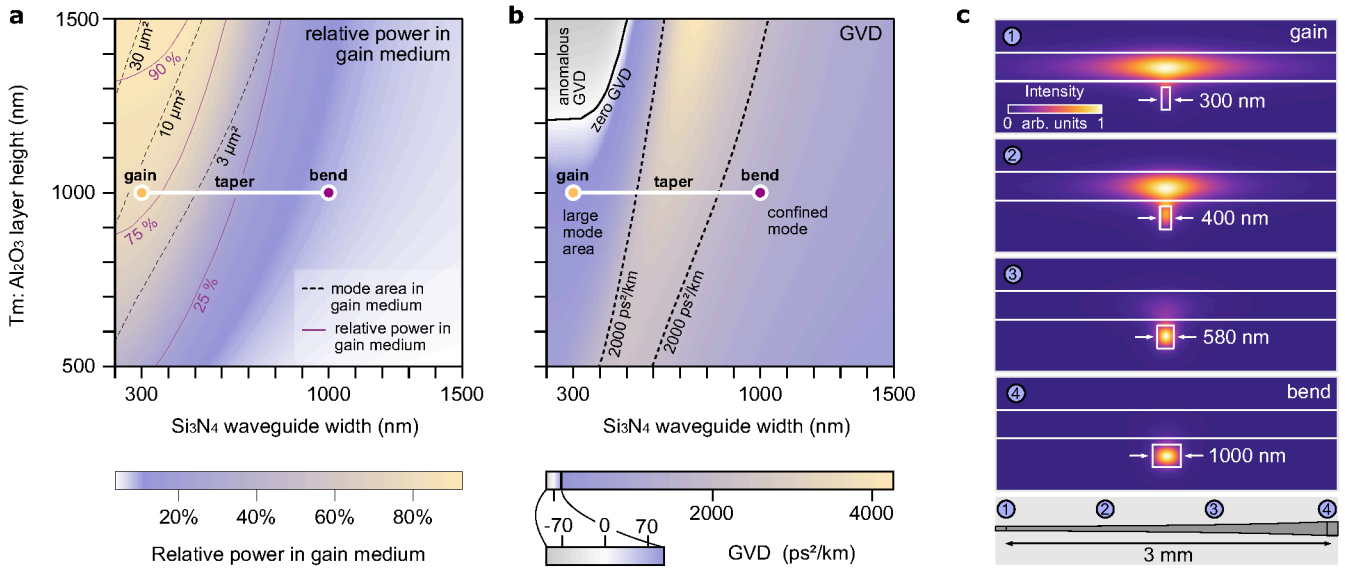

Figure 2 | Amplifier design. **a**, Relative power fraction in the transverse magnetic (TM) mode that is contained in the Tm^{3+}:Al_2O_3 gain layer (colorscale, purple contours) and mode-area in the in the gain layer (dashed black contours) in dependence of the Tm^{3+}:Al_2O_3 layer height and the Si_3N_4 waveguide width; cf. Methods for definition of the mode-area. The locations of the gain waveguides ("gain"), bends ("bend") and tapers ("taper") in the parameter space are indicated. **b**, Group velocity dispersion (GVD) (colorscale, dashed black contours); axes and labels as in (a). **c**, Simulated intensity profiles for different Si_3N_4 waveguide widths as they occur in gain, bent and tapered waveguide sections. Their positions along the adiabatic taper-profile are indicated. The simulations are based on a finite-element method model.

ready enabled Q-switched lasers with nanosecond pulse duration [42, 43]. In the curved sections the waveguide width is 1000 nm for strong mode confinement (Fig. 1e) and low-loss propagation; Euler-bends with a minimal radius of 200 µm guarantee an adiabatic low-loss transition to the bends [44].

The amplifying and bending waveguide sections are connected by straight adiabatically tapered waveguides. To increase mode confinement for low reflections and scattering at the cladding material transition, input and output waveguides are 2000 nm wide. Inverse tapers at the facets of the chip enable low-loss coupling from and to optical fibers or free-space. The footprint of the entire amplifier structure is below 15 mm^2. The choice of Tm-doping is motivated by its large gain bandwidth [21, 42, 43, 45, 46] and its importance for emerging applications such as laser ranging, free-space communication [47] and mid-infrared supercontinua [48]; however, the amplifier platform can also support erbium-doping for operation in the telecommunication wavelength window [49], and likely other rare-earth dopants such as neodymium and ytterbium for operation around 1 μm wavelength.

The design of the geometry of the amplifier is based on numerical simulation of key waveguide parameters obtained through a finite element electro-magnetic mode solver. For these simulations to be accurate, we utilize wavelength dependent refractive index data that was obtained for all involved materials through broadband ellipsometry. Fig. 2a,b show, for the fundamental transverse magnetic mode (TM), the relative optical power in the gain layer and the GVD as a function of the Si_3N_4 waveguide width and the Tm^{3+}:Al_2O_3 layer height. To achieve high gain and high saturation power, a large power fraction of the optical mode in the Tm^{3+}:Al_2O_3 layer is generally desirable. This also reduces the impact of nonlinear optical effects by (i) lowering the intensity through a large mode-area, (ii) a 10-fold reduced nonlinear material index of the gain layer compared to the silicon nitride waveguide, and (iii) by achieving high-gain amplification over short distances. However, a too large mode-area (and the correspondingly high number of excited ions) would increase the minimum signal input power required to avoid excessive spontaneous emission or parasitic lasing, particularly in a co-propagating (forward) pumping scheme. In addition to a high power fraction in the gain medium, we aim at an all-normal GVD along the entire amplifier structure to achieve monotonous temporal pulse compression and robustness against pulse breakup by nonlinear modulation instability (MI) [50]. As Fig. 2a and b show, it is indeed possible to simultaneously fulfill these criteria for the gain-waveguide, taper and bend for a Tm^{3+}:Al_2O_3 layer thickness below 1200 nm. Here, we use a chip with a layer thickness of 1000 nm in the normal GVD regime.

The location of the gain waveguide, bends and connecting tapers in the design parameter space are indicated in Fig. 2a,b and their mode profiles are shown in Fig. 2c. In this design the effective mode-area in the gain layer is $A_{\mathrm{eff}}^{\mathrm{gain}} \approx 7\ \mu m^2$ with an effective nonlinear parameter of $\gamma = 0.007\ W^{-1}m^{-1}$ (in the 1000 nm wide waveguide $\gamma = 0.7\ W^{-1}m^{-1}$) (see Methods). The group-delay dis-

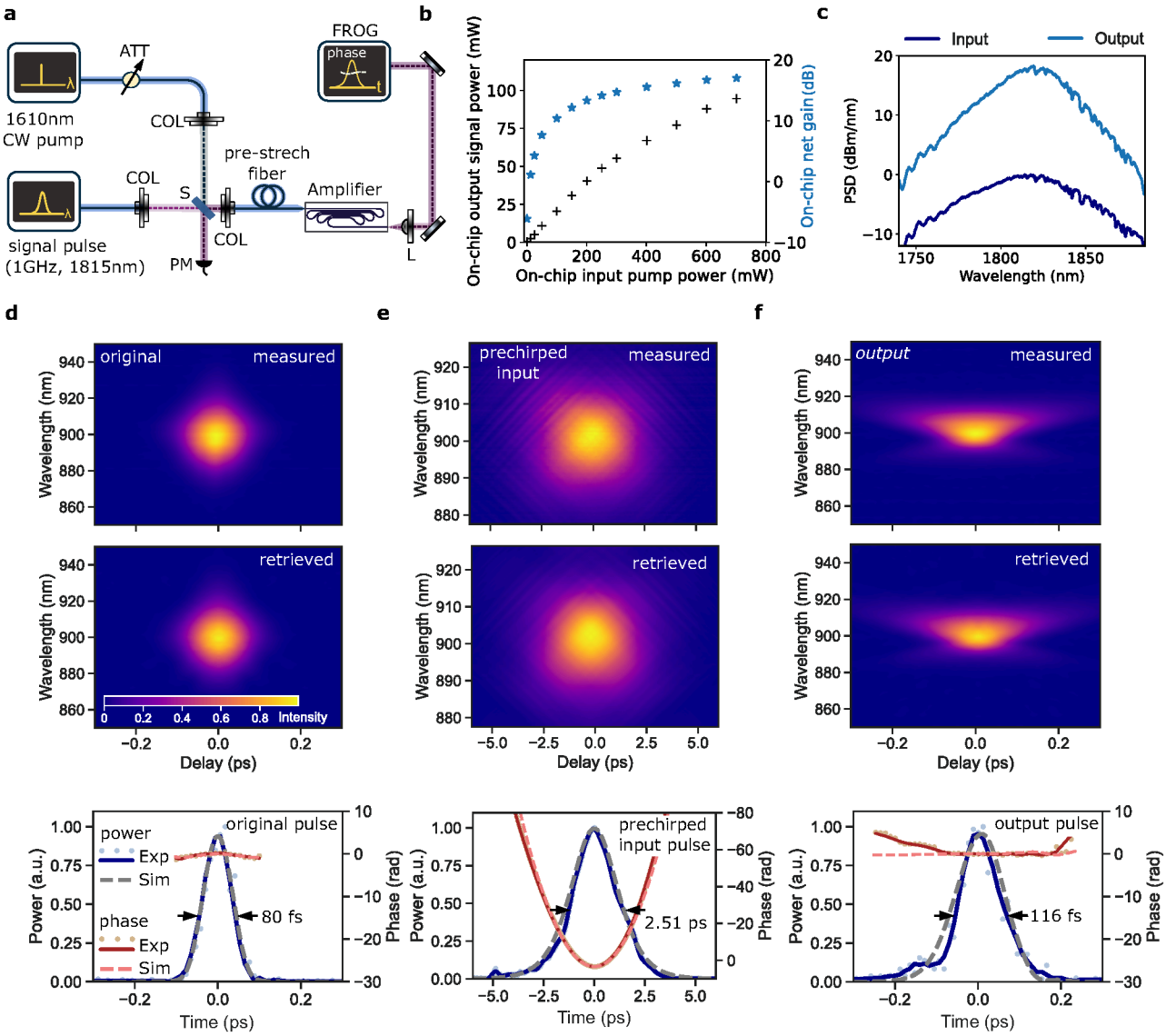

Figure 3 | **Experiments**. **a**, Experimental setup. CW: continuous-wave; ATT: attenuator; COL: collimator; S: beam-splitter; L: lens; PM: power-meter **b**, Amplifier output power and on-chip net gain as function of the on-chip pump power. **c**, Optical spectra before and after amplification; PSD: power spectral density. **d,e,f**, Frequency resolved optical gating (FROG) traces showing second harmonic intensity as function of FROG delay (256x256 data points) and reconstructed temporal pulse (power and phase) of the original, the pre-chirped input and the output pulses. Dots and solid lines represent measured and smoothed measured data, dashed lines represent simulated data. The respective FROG errors are $1.282{\cdot}10^{-5}$, $2.75{\cdot}10^{-6}$, and $1.19{\cdot}10^{-5}$.

persion (GDD, i.e. the length-integrated GVD) of the amplifier chip is $7.79{\cdot}10^{-26}$ s^2, which is large enough to allow pre-chirping to pico-second duration pulses. For ultrashort pulses, besides second order dispersion (GVD), third order disperison can be important. As we show in the Supplementary Information (SI, Section 1, Figure S1), the distinct third order dispersion characteristics of bends and tapers can be leveraged to minimize detrimental impacts of third order dispersion.

The experimental setup for testing the amplifier is shown in Fig. 3a, including the input signal pulse and the 1610 nm continuous-wave (CW) pump sources that are externally combined and coupled to the chip. For convenience, the pump source is here implemented via a diode laser that is amplified in an erbium-doped fiber amplifier. Future integration may utilize high power single-mode laser diodes, which are commercially available with power levels of larger than 400 mW, and which could be combined in a polarization multiplexed and/or bi-directional pumping configuration. Alternatively, 790 nm pump diodes may be used to excite the gain medium via power-efficient cross-relaxation processes; given the significance of Tm-doped gain materials, we anticipate high-power pump diodes to become readily available. The

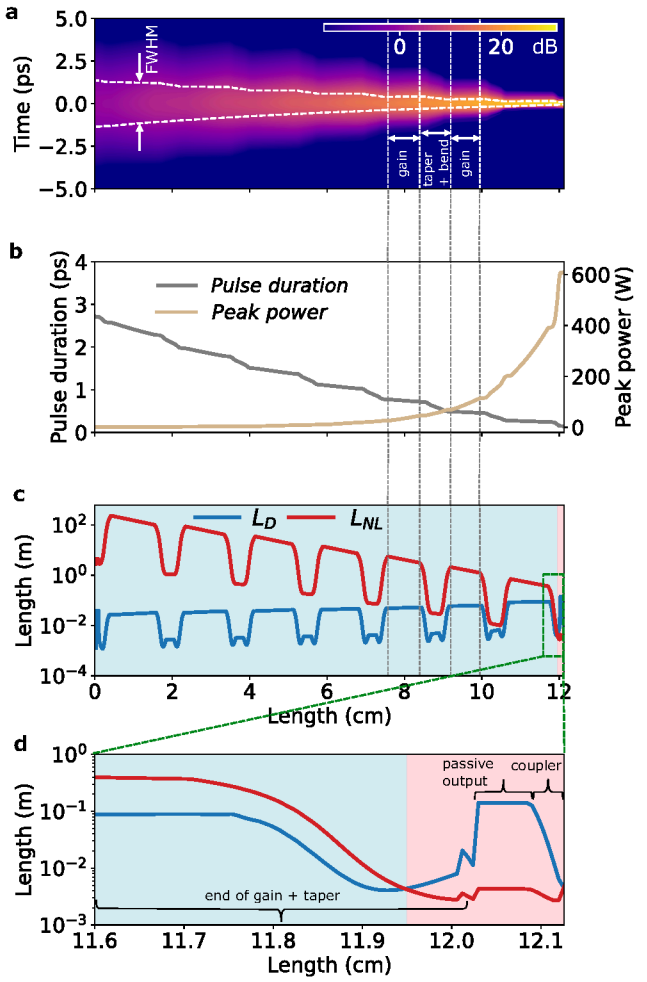

Figure 4 | **Numerical simulation**. **a**, Evolution of the temporal pulse power while propagating through the amplifier chip in a co-moving reference frame. One sequence of the alternating gain, bend and taper sections is indicated. The contours indicate the full-width-half-maximum (FWHM) pulse duration. **b**, Pulse duration and pulse peak power while propagating through the amplifier chip. **c**, Evolution of the pulse's dispersion length L_{D} and nonlinear length L_{NL} while propagating through the amplifier chip. The blue background color highlights where the propagation is dominated by linear optical effects ($L_{\mathrm{D}} < L_{\mathrm{NL}}$); nonlinear optical effects dominate only in the last 1.5 mm of the entire >12 cm long propagation distance (red background color). **d**, Magnified portion of panel c, where the gain section and taper to the output waveguide, the passive output waveguide, and the inverse taper for chip-output coupling are indicated. See Methods for details on the simulation.

output of the amplifier is collected via free-space optics to avoid additional dispersive or nonlinear optical effects and characterized via frequency resolved optical gating (FROG) [51]. As input pulse source we use a femtosecond laser source (cf. Methods) providing close to bandwidth-limited pulses of 80 fs duration at a central wavelength of 1815 nm and a pulse repetition rate of 1 GHz of which we couple 1.81 mW of average power (1.81 pJ pulse energy) to the chip. Prior to coupling the pulses to the chip, they are pre-chirped in a short stretch of standard anomalous dispersion optical fiber. The fiber can easily be adjusted in its length to explore different levels of pre-chirping. However, we emphasize that such pre-chirping can also be implemented on-chip without suffering from nonlinear effects owing to the low pulse energy prior to amplification. Relevant approaches include strongly anomalous dispersion waveguides [16], Bragg-gratings [52–54], or coupled gratings [55, 56].

As an aside, we note that it is in principle also possible to send the pulses directly, without pre-chirping, into the amplifier and to perform re-compression after the amplification (SI, Section 2, Fig. S2). However, this would require dispersion compensation at higher power levels after amplification, which, in contrast to pre-chirping at lower power, is challenging due to non-trivial nonlinear compression dynamics. If carefully optimized, self-similar nonlinear pulse amplification in the normal dispersion regime [57, 58] , followed by anomalous dispersion and/or nonlinear pulse compression may results in pulse shortening; however, this is not pursued here and only works for very specific input pulse parameters.

Fig. 3b shows the average power of the amplified pulses as well as the on-chip net gain for different levels of pump power. For the highest on-chip pump power of 700 mW, we observe an on-chip output signal power of 95 mW and a maximal gain of 17 dB, i.e. a factor of 52 (see Methods for details on calibration); the optical spectrum before and after amplification is shown in Fig. 3c. Next, we vary the length of the pre-chirping fiber and measure the temporal characteristics of the output pulses directly after the chip via FROG. For an optimal pre-chirping fiber length of 146.5 cm, commensurate with the opposite amount of total dispersion along the amplifier chip, we obtain an amplified and compressed pulse directly at the output facet of the chip of 116 fs duration. The temporal characterization of the original, pre-chirped and amplified pulses are shown in Fig. 3d,e and f, respectively. The pre-chirped pulses have a duration of 2.5 ps and a markedly quadratic temporal phase. In contrast, the output pulses of the amplifier are 116 fs in duration and exhibit a largely flat temporal phase indicating that they are close to time-bandwidth-limited. The asymmetric low intensity tail of the reconstructed pulse (and a 'butterfly' shape in the FROG trace) hints at a weak residual third order dispersion. In total, this experiment signifies the successful more than 50-fold amplification of a femtosecond pulse in an integrated photonic chip. The obtained on-chip pulse energy of 95 pJ and peak power of $>$ 800 W are well-suited for photonic chip-based spectral generation from infrared to ultraviolet wavelength [59, 60] or self-referencing [61] for absolute optical metrology. In integrated microwave photonics [62], ultrashort pulses could improve shot-noise limited performance by several orders of magnitude [63] with impact on navigation and communication applications. If higher average output power is needed, a longer amplifier structure and larger mode-area gain waveguides can be used.

We note that the final output pulses of 116 fs duration are longer than the 80 fs input pulse. This correlates well with their respective spectral bandwidth of 5.1 THz and 3.5 THz, respectively. We therefore attribute the increase in pulse duration to a finite gain bandwidth, but also to residual third order dispersion. Potentially, although less likely, nonlinear spectral compression could play a role [64].

Complementing the experiment, we perform numerical simulations of on-chip pulse amplification based on the nonlinear Schrödinger equation (NLSE) combined with a thulium gain model (see Methods). Using the experimental parameters of the input pulse, pump power and waveguide parameters, we simulate the pulse amplification and compare it with the experimental data in Fig. 3d,e,f (bottom). The simulation is in excellent agreement with the experimental observations and we can use it to gain further insights into the pulse propagation during the amplification process. Fig. 4a shows the simulated temporal dynamics of amplification and pulse shortening. We extract the pulse duration as a function of propagation distance and confirm the intended monotonous pulse compression that permits to keep the pulse peak power P_p and the impact of nonlinear effects low throughout most of the amplifier length (Fig. 4b). To illustrate this point, we plot in Fig. 4c the nonlinear length $L_\mathrm{NL} = (\gamma P_\mathrm{p})^{-1}$, the characteristic propagation length scale on which nonlinear effects become relevant. It can be seen that L_NL is consistently longer than the stretches of propagation to which it applies, indicating the limited impact of nonlinear effects. We also indicate the characteristic length scale of dispersive effects $L_\mathrm{D} = \mathrm{TBP}^2/(\Delta f^2|\mathrm{GVD}|)$, which is significantly shorter than L_NL for most of the propagation, confirming that pulse propagation is dominated by linear optical effects (Δf is the spectral bandwidth of the pulse as obtained from the simulation data at each point of the propagation and TBP is the time-bandwidth product, here set to 0.315).

Discussion

In summary, we have demonstrated ultrashort femtosecond pulse amplification in an integrated photonic chip. The central challenge of strong optical nonlinearity inherent to integrated photonics is effectively addressed through tailored large mode-area gain waveguides and the design of the waveguide's dispersion, permitting stable pulse propagation and compression, including in the tightly confining bends. The achieved 50-fold on-chip amplification leads to a peak power of 800 W. Longer amplifying waveguides and larger mode-area can support even higher average output power, accommodating higher pulse repetition rates. As we discuss in the SI (Section 3, Fig. S3), substantially increasing the peak power while avoiding nonlinear effects would require a design with increased waveguide dispersion, or shorter pulses which are, in principle, supported by the Tm-doped gain medium. Future work, may also leverage deliberate nonlinear effects such as self-similar pulse amplification in the normal dispersion regime [57, 58] followed by anomalous dispersion and potentially nonlinear compression to provide high-power few-cycle pulses [65]. As such, our results open new opportunities for scalable high-power fully-chip integrated ultrafast sources. More broadly, they bring femtosecond technology with pulse peak-power otherwise only attainable in table-top systems to the chip-level.

Methods

Sample fabrication. The passive Si_3N_4 chips were fabricated by Ligentec SA using UV optical lithography, based on a 800 nm-thick Si_3N_4 waveguide platform embedded in a silica cladding. In the area of the gain waveguides, the top silica cladding is removed (a 200 nm silica spacer layer remains). A Tm^{3+}: Al_2O_3 gain layer with a thickness of 1000 nm is then deposited in the local opening using radio frequency sputtering technique [66] with an estimated Tm^{3+} ion concentration of $3.5{\cdot}10^{20}\mathrm{cm}^{-3}$. The gain layer is cladded with a 1000 nm-thick silica layer on top for protection. Finally, the chip is annealed at 500 °C for 6 hours to reduce the OH and water absorption in the cladding layer.

Nonlinear coefficient and effective mode-area. The nonlinear coefficient γ of the waveguides is [67]

$$\gamma = \frac{\epsilon_0 \omega_s}{\mu_0 c} \frac{\iint n^2(x,y) n_2(x,y) |\mathbf{E}(\mathbf{x},\mathbf{y})|^4 \mathrm{d}x\mathrm{d}y}{\left| \iint \mathrm{Re}\left[\mathbf{E}(x,y) \times \mathbf{H}^*(x,y)\right]_z \mathrm{d}x\mathrm{d}y \right|^2}$$

where the integral extends over the entire heterogeneous material geometry. $\mathbf{E}$ and $\mathbf{H}$ are the complex electric and magnetic field vectors, x and y the transverse spatial coordinates. The effective mode-area $A_\mathrm{eff}^\mathrm{gain}$ in the homogeneous gain medium is

$$A_\mathrm{eff}^\mathrm{gain} = \frac{\left(\iint_\mathrm{gain} |\mathbf{E}(x,y)|^2 \mathrm{d}x\mathrm{d}y \right)^2}{\iint_\mathrm{gain} |\mathbf{E}(x,y)|^4 \mathrm{d}x\mathrm{d}y}$$

where the integration is restricted to the Tm^{3+}:Al_2O_3 gain layer.

Ultrafast signal source. 150 fs, 1 GHz pulses at 1560 nm are launched into a highly nonlinear fiber (HNLF) to generate a Raman-shifted soliton pulse centered at a wavelength of 1815 nm. A free-space 1700 nm long pass filter (LPF) is used to remove residual short wavelengths contributions.

Power calibration and gain measurements. Pump and signal fiber-to-chip coupling losses are measured using passive (no gain layer) waveguides and a symmetric lensed fibers configuration for input and output coupling. Measured pump and signal coupling losses are 2.9 and 4.2 dB per facet, respectively. We extract the net gain by directly comparing the output and input signal powers after calibrations and after filtering out the transmitted pump using a free-space long-pass filter.

Model for the amplification dynamics. Based on the NLSE, our model for propagation and amplification of the signal pulses combines effects of nonlinearity, gain and dispersion. The optical nonlinearity is treated in the time domain

$$\frac{\partial A_k(z)}{\partial z} = i\gamma |A_k(z)|^2 A_k(z),$$

where $A_k(z)$ is the complex temporal field amplitude of the signal, defined in the co-moving time frame on the discrete temporal points T_k $(k = 0, 1, 2, .., N-1)$ and normalized such that $\sum_k |A_k(z)|^2 \Delta T$ is the pulse energy at position z with $\Delta T = T_{k+1} - T_k$. Dispersion and gain are treated in the frequency domain

$$\frac{\partial \tilde{A}_j(z)}{\partial z} = \frac{g_{S,j}(z)}{2}\tilde{A}_j(z) + i\sum_{n\geq 2}\frac{\beta_n}{n!}(\omega_j - \omega_S)^n \tilde{A}_j(z)$$

where $\tilde{A}_j(z)$ is the discrete Fourier-transform of $A_k(z)$, with frequencies ω_j $(j = 0, 1, 2, .., N-1)$, and ω_S is the signal's center frequency. The frequency resolution is $\Delta\omega = \frac{2\pi}{N\Delta T}$, the signal gain is $g_{S,j}(z)$, and the β_n describe the dispersion.

We model the optical gain by accounting for the populations in the first three lower-lying levels ($^3H_6$, $^3F_4$ and $^3H_5$). The gain model also accounts for the fractions f_a and f_q of active and quenched ions ($f_a + f_q = 1$), respectively. Assuming a steady state for the gain medium, the rate equations including energy transfer upconversion (ETU) process for 1610 nm pumping are given by [18, 68]:

$$\begin{aligned}
\frac{dN_{2,a/q}(z)}{dt} =& W_{ETU} N_{1,a/q}^2(z) - \frac{1}{\tau_2} N_{2,a/q}(z) = 0\\
\frac{dN_{1,a/q}(z)}{dt} =& R_{P,a/q}(z) - R_{S,a/q}(z) - W_{ETU} N_{1,a/q}^2(z)\\
&+ \frac{1}{\tau_2} N_{2,a/q}(z) - \frac{1}{\tau_{1,a/q}} N_{1,a/q}(z) = 0\\
f_{a/q}(z) N_d =& N_{0,a/q}(z) + N_{1,a/q}(z) + N_{2,a/q}(z)\\
R_{P,a/q}(z) =& \frac{1}{\hbar\omega_P}\frac{P_P(z)}{A_{\text{eff}}(\omega_P)}\\
&\times\Big[\sigma_a(\omega_P) N_{0,a/q}(z) - \sigma_e(\omega_P) N_{1,a/q}(z)\Big]\\
R_{S,a/q}(z) =& \sum_j \frac{1}{\hbar\omega_S}\frac{P_{S,j}(z)}{A_{\text{eff}}(\omega_S)}\\
&\times\Big[\sigma_e(\omega_j) N_{1,a/q}(z) - \sigma_a(\omega_j) N_{0,a/q}(z)\Big]
\end{aligned}$$

where the concentrations $N_{0,1,2}$ describes the populations in the levels $^3H_6$, $^3F_4$ and $^3H_5$, respectively, the subscripts a/q denote the active or quenched ions and N_d is the total ion concentration; τ_i is the luminescence lifetime of level i and W_{ETU} is a parameter accounting for the ETU processes $^3F_4$, $^3F_4 \rightarrow {}^3H_5$, $^3H_6$ [18, 69]. $R_{p,a/q}$ and $R_{s,a/q}$ are the pump and signal rates. The pump power P_P is monochromatic with frequency ω_P and the signal power contained in the spectral discretization intervals is $P_{S,j}(z) = \frac{\Delta T^2}{T}|\tilde{A}_j(z)|^2 \frac{\Delta\omega}{2\pi} = N^{-2}|\tilde{A}_j(z)|^2$. For the pump and signal intensities, we neglect the transverse spatial intensity profiles (orthogonal to the propagation direction) and instead approximate them via effective mode areas $A_{\text{eff}}(\omega_P) \approx A_{\text{eff}}(\omega_S) \approx 7.5\,\mu\text{m}^2$. Further, σ_e and σ_a are the frequency dependent effective emission and absorption cross-sections and $\hbar$ is the reduced Planck constant. The propagation equations of the pump and signal power, which describe the gain along the propagation direction z are

$$\begin{aligned}
\frac{1}{P_P(z)}\frac{dP_P(z)}{dz} =& \Gamma_P\Big[\sigma_e(\omega_P)\Big(N_{2,a}(z) + N_{2,q}(z)\Big)\\
&- \sigma_a(\omega_P)\Big(N_{0,a}(z) + N_{0,q}(z)\Big)\Big] - \alpha
\end{aligned}$$

and

$$\begin{aligned}
\frac{1}{P_{S,j}(z)}\frac{dP_{S,j}(z)}{dz} =& \Gamma_S\Big[\sigma_e(\omega_j)\Big(N_{1,a}(z) + N_{1,q}(z)\Big)\\
&- \sigma_{s,a}(\omega_j)\Big(N_{0,a}(z) + N_{0,q}(z)\Big)\Big] - \alpha.
\end{aligned}$$

Here, Γ_S and Γ_P are the power fractions of signal and pump in the gain medium, respectively, and α describes the propagation loss which we assume to be the same for both pump and signal. While the pump propagation equation is used directly to model the evolution of $P_P(z)$, the evolution of the signal is modeled via its field amplitude as described above using $g_{S,j}(z) = \frac{1}{P_{S,j}(z)}\frac{dP_{S,j}(z)}{dz}$.

Acknowledgments

This project has received funding from Horizon 2020 research and innovation program (FEMTOCHIP, grant agreement No 965124 (M.G., F.X.K., S.M.G.B., T.H.)), from the European Research Council (ERC) under the EU's Horizon 2020 research and innovation program (STARCHIP, grant agreement No 853564 (T.H.); CounterLight, grant agreement No 756966(P.D.H.)), from the Deutsche Forschungsgemeinschaft (SP2111, contract number 403188360 (F.X.K.)), and through the Helmholtz Young Investigators Group VH-NG-1404 (T.H.); the work was supported through the Maxwell computational resources operated at DESY.

Author Contributions

M.A.G., T.W., T.H. designed the amplifier chip. M.A.G. developed and performed tests for gain waveguide development. M.A.G., M.L. designed and built the setup for pulse characterization, performed pulse amplification experiments and analyzed the data. T.V. contributed to the development of pulse input source. M.A.G. developed and performed the numerical simulations. H.F., M.G. fabricated the silicon nitride chip. K.W., S.M.G.B. developed and deposited the gain medium. S.Z., T.B., P.D.H. supported cladding development. M.S., J.L., N.S., F.X.K. contributed to the development of gain medium and amplifier. T.H. supervised the work. M.A.G., T.H. prepared the manuscript with input from all authors.

Competing interests

We declare that none of the authors have competing interests.

References

[1] Warren R. Zipfel, Rebecca M. Williams, and Watt W. Webb. Nonlinear magic: multiphoton microscopy in the biosciences. *Nature Biotechnology*, 21(11):1369–1377, November 2003. Number: 11 Publisher: Nature Publishing Group.

[2] Adam M. Larson. Multiphoton microscopy. *Nature Photonics*, 5(1):1–1, January 2011. Number: 1 Publisher: Nature Publishing Group.

[3] Hsiang-Yu Chung, Rüdiger Greinert, Franz X. Kärtner, and Guoqing Chang. Multimodal imaging platform for optical virtual skin biopsy enabled by a fiber-based two-color ultrafast laser source. *Biomedical Optics Express*, 10(2):514–525, February 2019. Publisher: Optica Publishing Group.

[4] A. M. Weiner, D. E. Leaird, Gary P. Wiederrecht, and Keith A. Nelson. Femtosecond Pulse Sequences Used for Optical Manipulation of Molecular Motion. *Science*, 247(4948):1317–1319, March 1990.

[5] Ahmed H. Zewail. Femtochemistry: Atomic-Scale Dynamics of the Chemical Bond. *The Journal of Physical Chemistry A*, 104(24):5660–5694, June 2000. Publisher: American Chemical Society.

[6] Nathalie Picqué and Theodor W. Hänsch. Frequency comb spectroscopy. *Nature Photonics*, 13(3):146–157, March 2019. Number: 3 Publisher: Nature Publishing Group.

[7] Tara Fortier and Esther Baumann. 20 years of developments in optical frequency comb technology and applications. *Communications Physics*, 2(1):1–16, December 2019. Number: 1 Publisher: Nature Publishing Group.

[8] Scott A. Diddams, Kerry Vahala, and Thomas Udem. Optical frequency combs: Coherently uniting the electromagnetic spectrum. *Science*, 369(6501):eaay3676, July 2020. Publisher: American Association for the Advancement of Science.

[9] Tobias J. Kippenberg, Alexander L. Gaeta, Michal Lipson, and Michael L. Gorodetsky. Dissipative Kerr solitons in optical microresonators. *Science*, 361(6402):eaan8083, August 2018.

[10] Alessia Pasquazi, Marco Peccianti, Luca Razzari, David J. Moss, Stéphane Coen, Miro Erkintalo, Yanne K. Chembo, Tobias Hansson, Stefan Wabnitz, Pascal Del'Haye, Xiaoxiao Xue, Andrew M. Weiner, and Roberto Morandotti. Micro-combs: A novel generation of optical sources. *Physics Reports*, 729:1–81, January 2018.

[11] Alexander L. Gaeta, Michal Lipson, and Tobias J. Kippenberg. Photonic-chip-based frequency combs. *Nature Photonics*, 13(3):158–169, March 2019. Number: 3 Publisher: Nature Publishing Group.

[12] K. Van Gasse, S. Uvin, V. Moskalenko, S. Latkowski, G. Roelkens, E. Bente, and B. kuyken. Recent Advances in the Photonic Integration of Mode-Locked Laser Diodes. *IEEE Photonics Technology Letters*, 31(23):1870–1873, December 2019.

[13] Lin Chang, Songtao Liu, and John E. Bowers. Integrated optical frequency comb technologies. *Nature Photonics*, 16(2):95–108, February 2022. Number: 2 Publisher: Nature Publishing Group.

[14] Neetesh Singh, Erich Ippen, and Franz X. Kärtner. Towards CW modelocked laser on chip – large mode area and NLI for stretched pulse mode locking. *Optics Express*, 28(15):22562, July 2020.

[15] Qiushi Guo, Benjamin K. Gutierrez, Ryoto Sekine, Robert M. Gray, James A. Williams, Luis Ledezma, Luis Costa, Arkadev Roy, Selina Zhou, Mingchen Liu, and Alireza Marandi. Ultrafast mode-locked laser in nanophotonic lithium niobate. *Science*, 382(6671):708–713, November 2023.

[16] Mengjie Yu, David Barton III, Rebecca Cheng, Christian Reimer, Prashanta Kharel, Lingyan He, Linbo Shao, Di Zhu, Yaowen Hu, Hannah R. Grant, Leif Johansson, Yoshitomo Okawachi, Alexander L. Gaeta, Mian Zhang, and Marko Lončar. Integrated femtosecond pulse generator on thin-film lithium niobate. *Nature*, 612(7939):252–258, December 2022.

[17] Laura Agazzi, Jonathan D. B. Bradley, Meindert Dijkstra, Feridun Ay, Gunther Roelkens, Roel Baets, Kerstin Wörhoff, and Markus Pollnau. Monolithic integration of erbium-doped amplifiers with silicon-on-insulator waveguides. *Opt. Express*, 18(26):27703, December 2010.

[18] Sergio A. Vázquez-Córdova, Meindert Dijkstra, Edward H. Bernhardi, Feridun Ay, Kerstin Wörhoff, Jennifer L. Herek, Sonia M. García-Blanco, and Markus Pollnau. Erbium-doped spiral amplifiers with 20 dB of net gain on silicon. *Optics Express*, 22(21):25993–26004, October 2014. Publisher: Optical Society of America.

[19] Hao Sun, Leijun Yin, Zhicheng Liu, Yize Zheng, Fan Fan, Shilong Zhao, Xue Feng, Yongzhuo Li, and C. Z. Ning. Giant optical gain in a single-crystal erbium chloride silicate nanowire. *Nature Photonics*, 11(9):589–593, September 2017.

[20] John Rönn, Weiwei Zhang, Anton Autere, Xavier Leroux, Lasse Pakarinen, Carlos Alonso-Ramos, Antti Säynätjoki, Harri Lipsanen, Laurent Vivien, Eric Cassan, and Zhipei Sun. Ultra-high on-chip optical gain in erbium-based hybrid slot waveguides. *Nature Communications*, 10(1):432, January 2019.

[21] Khadijeh Miarabbas Kiani, Henry C. Frankis, Hamidu M. Mbonde, Richard Mateman, Arne Leinse, Andrew P. Knights, and Jonathan D. B. Bradley. Thulium-doped tellurium oxide waveguide amplifier with 7.6 dB net gain on a silicon nitride chip. *Optics Letters*, 44(23):5788, December 2019.

[22] Henry C. Frankis, Hamidu M. Mbonde, Dawson B. Bonneville, Chenglin Zhang, Richard Mateman, Arne Leinse, and Jonathan D. B. Bradley. Erbium-doped TeO_2-coated Si_3N_4 waveguide amplifiers with 5 dB net gain. *Photonics Research*, 8(2):127–134, February 2020. Publisher: Optical Society of America.

[23] Jinfeng Mu, Meindert Dijkstra, Jeroen Korterik, Herman Offerhaus, and Sonia M. García-Blanco. High-gain waveguide amplifiers in Si_3N_4 technology via double-layer monolithic integration. *Photonics Research*, 8(10):1634, October 2020.

[24] John Rönn, Jianhao Zhang, Weiwei Zhang, Zhengrui Tu, Antti Matikainen, Xavier Leroux, Elena Durán-Valdeiglesias, Nathalie Vulliet, Frederic Boeuf, Carlos Alonso-Ramos, Harri Lipsanen, Laurent Vivien, Zhipei Sun, and Eric Cassan. Erbium-doped hybrid waveguide amplifiers with net optical gain on a fully industrial 300 mm silicon nitride photonic platform. *Optics Express*, 28(19):27919, September 2020.

[25] Yang Liu, Zheru Qiu, Xinru Ji, Anton Lukashchuk, Jijun He, Johann Riemensberger, Martin Hafermann, Rui Ning Wang, Junqiu Liu, Carsten Ronning, and Tobias J. Kippenberg. A photonic integrated circuit–based erbium-doped amplifier. *Science*, 376(6599):1309–1313, June 2022.

[26] Yuechen Jia, Jiangwei Wu, Xiaoli Sun, Xiongshuo Yan, Ranran Xie, Lei Wang, Yuping Chen, and Feng Chen. Integrated Photonics Based on Rare-Earth Ion-Doped Thin-Film Lithium Niobate. *Laser & Photonics Reviews*, 16(9):2200059, September 2022.

[27] Neetesh Singh, Jan Lorenzen, Milan Sinobad, Kai Wang, Mahmoud A. Gaafar, Henry Francis, Michael Geiselmann, Tobias Herr, Sonia M Garcia-Blanco, and Franz X. Kärtner. Watt-Class CMOS-Compatible Power Amplifier, June arXiv:2306.12940 [physics.optics] (2023).

[28] Michael L. Davenport, Sandra Skendzic, Nicolas Volet, Jared C. Hulme, Martijn J. R. Heck, and John E. Bowers. Heterogeneous Silicon/III–V Semiconductor Optical Amplifiers. *IEEE Journal of Selected Topics in Quantum Electronics*, 22(6):78–88, November 2016.

[29] Michael L. Davenport, Songtao Liu, and John E. Bowers. Integrated heterogeneous silicon/III–V mode-locked lasers. *Photonics Research*, 6(5):468, May 2018.

[30] Kasper Van Gasse, Ruijun Wang, and Gunther Roelkens. 27 dB gain III–V-on-silicon semiconductor optical amplifier with $>$ 17 dBm output power. *Optics Express*, 27(1):293, January 2019.

[31] Camiel Op de Beeck, Bahawal Haq, Lukas Elsinger, Agnieszka Gocalinska, Emanuele Pelucchi, Brian Corbett, Günther Roelkens, and Bart Kuyken. Heterogeneous III-V on silicon nitride amplifiers and lasers via microtransfer printing. *Optica*, 7(5):386, May 2020.

[32] Ju Won Choi, Byoung-Uk Sohn, Ezgi Sahin, George F. R. Chen, Peng Xing, Doris K. T. Ng, Benjamin J. Eggleton, and Dawn T. H. Tan. An optical parametric Bragg amplifier on a CMOS chip. *Nanophotonics*, 10(13):3507–3518, October 2021.

[33] Luis Ledezma, Ryoto Sekine, Qiushi Guo, Rajveer Nehra, Saman Jahani, and Alireza Marandi. Intense optical parametric amplification in dispersion-engineered nanophotonic lithium niobate waveguides. *Optica*, 9(3):303, March 2022.

[34] Johann Riemensberger, Nikolai Kuznetsov, Junqiu Liu, Jijun He, Rui Ning Wang, and Tobias J. Kippenberg. A photonic integrated continuous-travelling-wave parametric amplifier. *Nature*, 612(7938):56–61, December 2022.

[35] J. Leuthold, C. Koos, and W. Freude. Nonlinear silicon photonics. *Nature Photon*, 4(8):535–544, August 2010.

[36] John M. Dudley, Goëry Genty, and Stéphane Coen. Supercontinuum generation in photonic crystal fiber. *Reviews of Modern Physics*, 78(4):1135–1184, October 2006.

[37] Michael R. E. Lamont, Barry Luther-Davies, Duk-Yong Choi, Steve Madden, and Benjamin J. Eggleton. Supercontinuum generation in dispersion engineered highly nonlinear (γ=10/W/m) As_2S_3 chalcogenide planar waveguide. *Optics Express*, 16(19):14938–14944, September 2008. Publisher: Optica Publishing Group.

[38] Bart Kuyken, Xiaoping Liu, Richard M. Osgood, Roel Baets, Günther Roelkens, and William M. J. Green. Mid-infrared to telecom-band supercontinuum generation in highly nonlinear silicon-on-insulator wire waveguides. *Optics Express*, 19(21):20172–20181, October 2011. Publisher: Optica Publishing Group.

[39] R. Halir, Y. Okawachi, J. S. Levy, M. A. Foster, M. Lipson, and A. L. Gaeta. Ultrabroadband supercontinuum generation in a CMOS-compatible platform. *Optics Letters*, 37(10):1685–1687, May 2012. Publisher: Optica Publishing Group.

[40] R M Wood, R T Taylor, and R L Rouse. Laser damage in optical materials at 1.06 μm. *Optics & Laser Technology*, 7:105–111, 1975.

[41] Donna Strickland and Gerard Mourou. Compression of amplified chirped optical pulses. *Optics Communications*, 56(3):219–221, 1985.

[42] Katia Shtyrkova, Patrick T. Callahan, Nanxi Li, Emir Salih Magden, Alfonso Ruocco, Diedrik Vermeulen, Franz X. Kärtner, Michael R. Watts, and Erich P. Ippen. Integrated CMOS-compatible Q-switched mode-locked lasers at 1900nm with an on-chip artificial saturable absorber. *Optics Express*, 27(3):3542, February 2019.

[43] Neetesh Singh, Jan Lorenzen, Milan Sinobad, Kai Wang, Andreas C. Liapis, Henry C. Frankis, Stefanie Haugg, Henry Francis, Jose Carreira, Michael Geiselmann, Mahmoud A. Gaafar, Tobias Herr, Jonathan D. B. Bradley, Zhipei Sun, Sonia M. Garcia-Blanco, and Franz X. Kärtner. Silicon photonics-based high-energy passively Q-switched laser. *Nature Photonics*, February 2024.

[44] Florian Vogelbacher, Stefan Nevlacsil, Martin Sagmeister, Jochen Kraft, Karl Unterrainer, and Rainer Hainberger. Analysis of silicon nitride partial Euler waveguide bends. *Optics Express*, 27(22):31394, October 2019.

[45] Zhan Su, Nanxi Li, E. Salih Magden, Matthew Byrd, Purnawirman, Thomas N. Adam, Gerald Leake, Douglas Coolbaugh, Jonathan D. B. Bradley, and Michael R. Watts. Ultra-compact and low-threshold thulium microcavity laser monolithically integrated on silicon. *Optics Letters*, 41(24):5708, December 2016.

[46] Nanxi Li, Purnawirman, Zhan Su, E. Salih Magden, Patrick T. Callahan, Katia Shtyrkova, Ming Xin, Alfonso Ruocco, Christopher Baiocco, Erich P. Ippen, Franz X. Kärtner, Jonathan D. B. Bradley, Diedrik Vermeulen, and

Michael R. Watts. High-power thulium lasers on a silicon photonics platform. *Optics Letters*, 42(6):1181, March 2017.

[47] Z. Li, A. M. Heidt, J. M. O. Daniel, Y. Jung, S. U. Alam, and D. J. Richardson. Thulium-doped fiber amplifier for optical communications at 2 µm. *Optics Express*, 21(8):9289, April 2013.

[48] Jiaqi Luo, Biao Sun, Jiayun Liu, Zhiyu Yan, Nanxi Li, Eng Leong Tan, Qijie Wang, and Xia Yu. Mid-IR supercontinuum pumped by femtosecond pulses from thulium doped all-fiber amplifier. *Optics Express*, 24(13):13939, June 2016.

[49] Dawson B. Bonneville, Ward A. P. M. Hendriks, Carlos E. Osornio-Martínez, Sohelia Mardani, Kai Wang, Anne M. Dijkstra, and Sonia M. García-Blanco. On-chip photonics erbium-doped amplifiers: fabrication and characterization of Al2O3:Er3+ and development as a laser platform. In Maurizio Ferrari, Angela B. Seddon, and Stefano Taccheo, editors, *Fiber Lasers and Glass Photonics: Materials through Applications III*, volume PC12142, page PC121420J. International Society for Optics and Photonics, SPIE, 2022.

[50] John M. Dudley, Frédéric Dias, Miro Erkintalo, and Goëry Genty. Instabilities, breathers and rogue waves in optics. *Nature Photonics*, 8(10):755–764, October 2014.

[51] Rick Trebino, Kenneth W. DeLong, David N. Fittinghoff, John N. Sweetser, Marco A. Krumbügel, Bruce A. Richman, and Daniel J. Kane. Measuring ultrashort laser pulses in the time-frequency domain using frequency-resolved optical gating. *Review of Scientific Instruments*, 68(9):3277–3295, September 1997.

[52] Zhenmin Du, Chao Xiang, Tingzhao Fu, Minghua Chen, Sigang Yang, John E. Bowers, and Hongwei Chen. Silicon nitride chirped spiral Bragg grating with large group delay. *APL Photonics*, 5(10):101302, October 2020.

[53] E. Sahin, K. J. A. Ooi, C. E. Png, and D. T. H. Tan. Large, scalable dispersion engineering using cladding-modulated Bragg gratings on a silicon chip. *Applied Physics Letters*, 110(16):161113, April 2017.

[54] Yaoshuai Li, Liang Xu, Danlu Wang, Qingzhong Huang, Chi Zhang, and Xinliang Zhang. Large group delay and low loss optical delay line based on chirped waveguide Bragg gratings. *Optics Express*, 31(3):4630, January 2023.

[55] Ju Won Choi, Ezgi Sahin, Byoung-Uk Sohn, George F. R. Chen, Doris K. T. Ng, Anuradha M. Agarwal, Lionel C. Kimerling, and Dawn T. H. Tan. High spectro-temporal compression on a nonlinear CMOS-chip. *Light: Science & Applications*, 10(1):130, June 2021.

[56] Dawn T.H. Tan, Pang C. Sun, and Yeshaiahu Fainman. Monolithic nonlinear pulse compressor on a silicon chip. *Nature Communications*, 1(1):116, November 2010.

[57] M. E. Fermann, V. I. Kruglov, B. C. Thomsen, J. M. Dudley, and J. D. Harvey. Self-Similar Propagation and Amplification of Parabolic Pulses in Optical Fibers. *Physical Review Letters*, 84(26):6010–6013, June 2000.

[58] John M. Dudley, Christophe Finot, David J. Richardson, and Guy Millot. Self-similarity in ultrafast nonlinear optics. *Nature Physics*, 3(9):597–603, September 2007.

[59] Tsung-Han Wu, Luis Ledezma, Connor Fredrick, Pooja Sekhar, Ryoto Sekine, Qiushi Guo, Ryan M. Briggs, Alireza Marandi, and Scott A. Diddams. Visible to Ultraviolet Frequency Comb Generation in Lithium Niobate Nanophotonic Waveguides, May arXiv:2305.08006 [astro-ph, physics:physics] (2023). arXiv:2305.08006 [astro-ph, physics:physics].

[60] Markus Ludwig, Furkan Ayhan, Tobias M. Schmidt, Thibault Wildi, Thibault Voumard, Roman Blum, Zhichao Ye, Fuchuan Lei, François Wildi, Francesco Pepe, Mahmoud A. Gaafar, Ewelina Obrzud, Davide Grassani, François Moreau, Bruno Chazelas, Rico Sottile, Victor Torres-Company, Victor Brasch, Luis G. Villanueva, François Bouchy, and Tobias Herr. Ultraviolet astronomical spectrograph calibration with laser frequency combs from nanophotonic waveguides, June arXiv:2306.13609 [astro-ph, physics:physics] (2023). arXiv:2306.13609 [astro-ph, physics:physics].

[61] Adrea R. Johnson, Aline S. Mayer, Alexander Klenner, Kevin Luke, Erin S. Lamb, Michael R. E. Lamont, Chaitanya Joshi, Yoshitomo Okawachi, Frank W. Wise, Michal Lipson, Ursula Keller, and Alexander L. Gaeta. Octave-spanning coherent supercontinuum generation in a silicon nitride waveguide. *Optics Letters*, 40(21):5117–5120, November 2015. Publisher: Optica Publishing Group.

[62] David Marpaung, Jianping Yao, and José Capmany. Integrated microwave photonics. *Nature Photon*, 13(2):80–90, February 2019.

[63] F. Quinlan, T. M. Fortier, H. Jiang, A. Hati, C. Nelson, Y. Fu, J. C. Campbell, and S. A. Diddams. Exploiting shot noise correlations in the photodetection of ultrashort optical pulse trains. *Nature Photonics*, 7(4):290–293, April 2013. Number: 4 Publisher: Nature Publishing Group.

[64] Sonia Boscolo, Frederic Chaussard, Esben Andresen, Hervé Rigneault, and Christophe Finot. Impact of initial pulse shape on the nonlinear spectral compression in optical fibre. *Optics & Laser Technology*, 99:301–309, February 2018.

[65] David R. Carlson, Phillips Hutchison, Daniel D. Hickstein, and Scott B. Papp. Generating few-cycle pulses with integrated nonlinear photonics. *Optics Express*, 27(26):37374, December 2019.

[66] Carlijn I. van Emmerik, Ward A. P. M. Hendriks, Martijn M. Stok, Michiel de Goede, Lantian Chang, Meindert Dijkstra, Frans Segerink, Dominic Post, Enrico G. Keim, Mike J. Dikkers, and Sonia M. García-Blanco. Relative oxidation state of the target as guideline for depositing optical quality RF reactive magnetron sputtered Al_2O_3 layers. *Optical Materials Express*, 10(6):1451, June 2020.

[67] C. Koos, L. Jacome, C. Poulton, J. Leuthold, and W. Freude. Nonlinear silicon-on-insulator waveguides for all-optical signal processing. *Opt. Express*, 15(10):5976, May 2007.

[68] L. Agazzi, K. Wörhoff, and M. Pollnau. Energy-Transfer-Upconversion Models, Their Applicability and Breakdown in the Presence of Spectroscopically Distinct Ion Classes: A Case Study in Amorphous Al2O3:Er3+. *The Journal of Physical Chemistry C*, 117(13):6759–6776, April 2013.

[69] Pavel Loiko and Markus Pollnau. Stochastic Model of Energy-Transfer Processes Among Rare-Earth Ions. Example of Al_2O_3:Tm^{3+}. *The Journal of Physical Chemistry C*, 120(46):26480–26489, November 2016.

Supplementary Information - Femtosecond pulse amplification on a chip

Mahmoud A. Gaafar[1,*], Markus Ludwig[1,*], Kai Wang[2], Thibault Wildi[1], Thibault Voumard [1], Milan Sinobad[1], Jan Lorenzen[1], Henry Francis[3], Jose Carreira[3], Shuangyou Zhang[4], Toby Bi[4,5], Pascal Del'Haye[4,5], Michael Geiselmann[3], Neetesh Singh[1], Franz X. Kärtner[1,6], Sonia M. Garcia-Blanco[2], Tobias Herr[1,6,**]

[1]Deutsches Elektronen-Synchrotron DESY, Notkestr. 85, 22607 Hamburg, Germany
[2]Integrated Optical Systems, MESA+ Institute for Nanotechnology, University of Twente, 7500AE, Enschede, The Netherlands
[3]LIGENTEC SA, EPFL Innovation Park, Chemin de la Dent-d'Oche 1B, Switzerland CH-1024 Ecublens, Switzerland
[4] Max-Planck Institute for the Science of Light, 91058 Erlangen, Staudtstr. 2, Germany
[5] Department of Physics, FAU Erlangen-Nürnberg, 91058 Erlangen, Germany
[6] Department of Physics, Universität Hamburg, Luruper Chaussee 149, 22761 Hamburg, Germany
[*]These authors contributed equally.
[**]tobias.herr@desy.de

1 Third order dispersion

For ultra-short pulses in the femtosecond regime, their large spectral bandwidth implies that third order dispersion effects become relevant. In our case, as evident in Fig. 3f in the main text, not perfectly compensated third order dispersion after compression leads to an asymmetric low intensity tail in the output pulse (and a 'butterfly' shape in the FROG trace). Complementing main text Fig. 2b, Figure S1 shows the third order dispersion in dependence of the silicon nitride waveguide width an the Al_2O_3 layer height. While the gain waveguides show close to zero third order dispersion, waveguide bends and tapers can exhibit considerable amounts of third order dispersion. Importantly, *both* signs of third order dispersion occur along the taper, so that they can compensate each other. In our case, although peak dispersion values exceeding 10 ps^3/km occur along the taper and during the bend, their mean value is much smaller and the different contributions approximately compensate each other (mean third order dispersion along a taper ca. 1.6 ps^3/km; mean dispersion in a bend ca. 7 ps^3/km; per straight gain waveguide the amplifier comprises ca. 2×3 mm of taper and a bend length of ca. 1.5 mm).

2 Amplification without pre-chirping

As mentioned in the main text, it is also possible to send the input pulses directly into the amplifier without pre-chirping. Due to the normal dispersion the pulses will spread in time before their gain in energy would cause substantial nonlinear effects. Figure S2 presents a numerical simulation of signal pulse amplification without pre-chirping the pulse, in the same representation as Fig. 4 in the main text). Figure S2a reveals the temporal dynamics of amplification and pulse broadening due to normal dispersion of the amplifier. To obtain short pulses, dispersion compensation would now be required after amplification, at higher power levels. In contrast to pre-chirping at low power, this is more challenging due to the non-trivial power-dependent nonlinear compression dynamics.

3 Critical power: $L_{\mathrm{NL}} = L_{\mathrm{D}}$

To provide an estimate of the maximally attainable peak power in a linear pulse propagation regime, we consider the critical power where nonlinear and dispersion length are equal $L_{\mathrm{NL}} = L_{\mathrm{D}}$. Figure S3 shows this critical power for different pulse duration (impacting L_{D}) and gain layer height (impacting L_{D} and L_{NL}), where we have assumed a fixed silicon nitride waveguide width of 300 nm. Figure S3 shows that a ∼100 fs pulse can be amplified and compressed to its time bandwidth limit with peak power levels of approximately 900 W, while remaining in the linear pulse propagation regime. For higher peak power levels nonlinearity will start contributing. Shorter pulses, which can in principle be supported by the Tm-doped gain medium could support higher peak power, in principle exceeding 10 kW, while remaining in the linear regime. To reach these power levels a careful management of higher order dispersion would be needed.

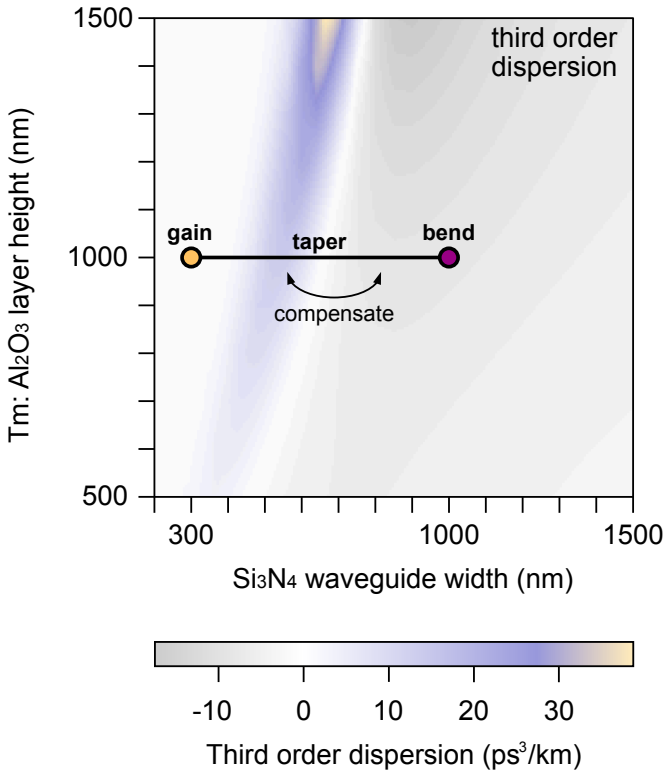

Figure S1 | **Third order dispersion** in dependence of the silicon nitride waveguide width an the Al_2O_3 layer height. Along the taper, both negative and positive third order dispersion are present and can compensate each other. Specifically, the taper profile may be chosen to obtain a net-zero third order dispersion amplifier.

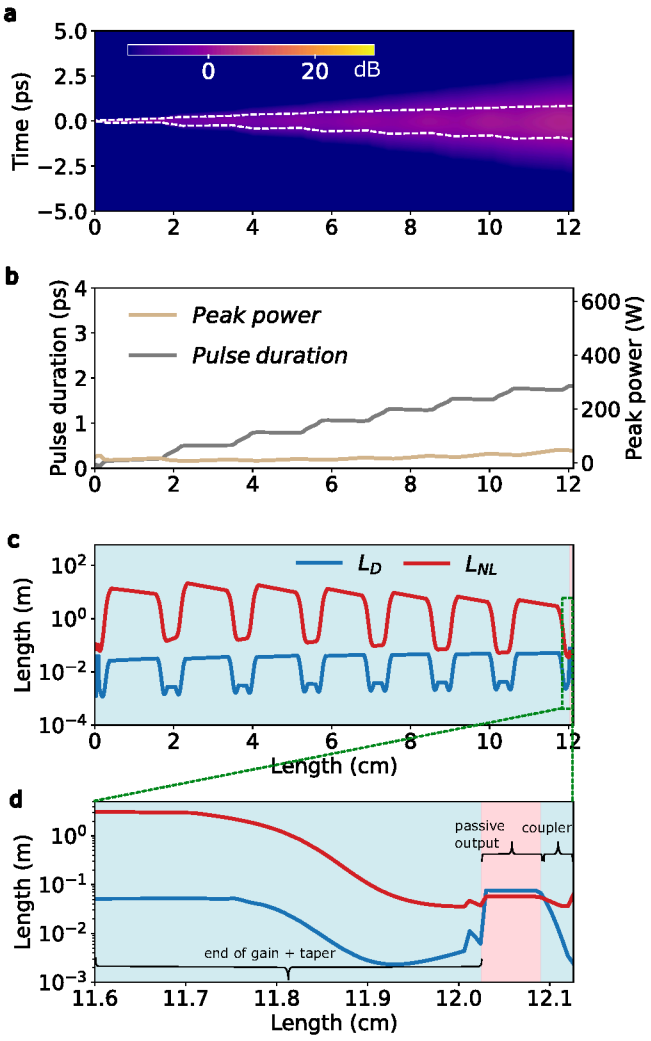

Figure S2 | Numerical simulation of signal amplification without pre-chirping. **a**, Evolution of the temporal pulse power while propagating through the amplifier chip in a co-moving reference frame. One sequence of the alternating gain, bend and taper sections is indicated. The contours indicate the full-width-half-maximum (FWHM) pulse duration. **b**, Pulse duration and pulse peak power while propagating through the amplifier chip. **c**, Evolution of the pulse's dispersion length L_{D} and nonlinear length L_{NL} while propagating through the amplifier chip. The blue background color highlights where the propagation is dominated by linear optical effects ($L_{\mathrm{D}} < L_{\mathrm{NL}}$); nonlinear optical effects dominate only in short section within the last 1.5 mm of the entire, $>$12 cm long propagation distance (red background color). **d**, shows a magnified portion of panel c., where the gain section and taper to the output waveguide, the passive output waveguide, and the inverse taper for chip-output coupling are indicated.

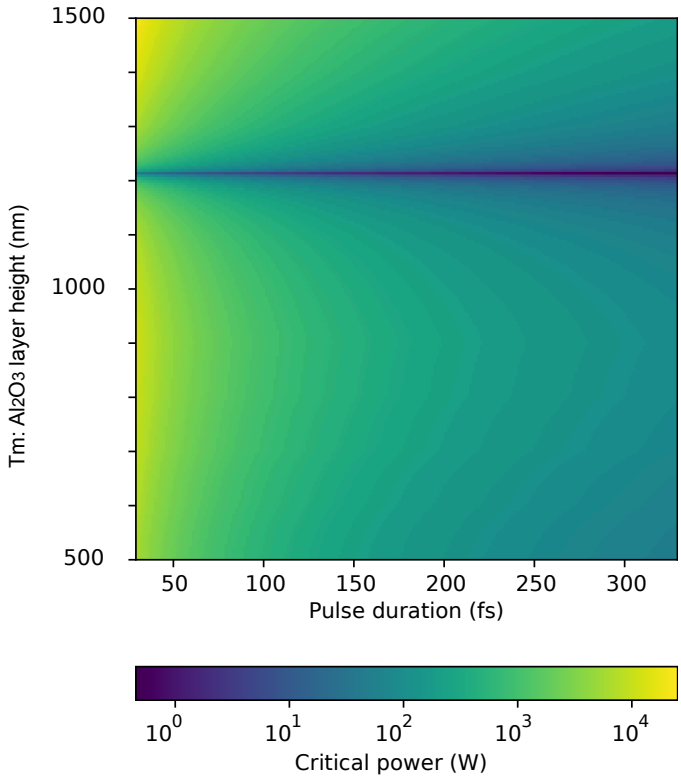

Figure S3 | **Critical power** in dependence of the pulse duration and the Al_2O_3 layer height (assuming 300 nm wide silicon nitride waveguide). The achievable peak power scales quadratically with the inverse pulse duration and linearly with the (absolute) value of the GVD. For a layer height of ~ 1200 nm, the GVD is close to zero and hence the critical power low. Higher critical power is achieved for shorter pulses and layer heights that exhibit larger GVD (cf. Fig. 2b in the main text).